

## Nature of the ring current in Saturn's dayside magnetosphere

S. Kellett,<sup>1</sup> C. S. Arridge,<sup>2,3</sup> E. J. Bunce,<sup>1</sup> A. J. Coates,<sup>2,3</sup> S. W. H. Cowley,<sup>1</sup>  
M. K. Dougherty,<sup>4</sup> A. M. Persoon,<sup>5</sup> N. Sergis,<sup>6</sup> and R. J. Wilson<sup>7</sup>

Received 30 November 2009; revised 9 February 2010; accepted 11 March 2010; published 4 August 2010.

[1] We employ magnetic field and plasma particle data from two equatorial passes of the Cassini spacecraft spanning the radial range between  $\sim 3$  and  $\sim 20 R_S$  to investigate the nature of the ring current in Saturn's dayside magnetosphere ( $R_S$  is Saturn's equatorial radius, equal to 60,268 km). We examine plasma parameters obtained by Cassini for each pass and compare the azimuthal current density profiles deduced with those obtained from current disk modeling of the magnetic field perturbations. We show that the current associated with the  $P_{\perp} > P_{\parallel}$  pressure anisotropy of the warm water group ions is important inside  $\sim 10 R_S$ , canceling a significant fraction of the otherwise dominant inertia current inside  $\sim 6 R_S$ . The overall total current density profile is then found to be similar to that produced by the pressure gradient current but augmented in strength by factors of  $\sim 1.5$ – $2.0$  by the difference between the inertia and anisotropy currents. The total current density rises from small values near  $\sim 6 R_S$ , peaks at  $\sim 100 \text{ pA m}^{-2}$  near  $\sim 8 R_S$ , and reduces to values below  $\sim 25 \text{ pA m}^{-2}$  at distances beyond  $\sim 15 R_S$ , up to the  $20 R_S$  limit of our study. The deduced current density profiles are in good agreement with the gross features of the profiles deduced from current disk modeling, with peak values occurring just outside the inner edge of the best fit models at  $\sim 7 R_S$ , though with the current density then falling more steeply with radial distance than the  $1/r$  dependence assumed in the model.

**Citation:** Kellett, S., C. S. Arridge, E. J. Bunce, A. J. Coates, S. W. H. Cowley, M. K. Dougherty, A. M. Persoon, N. Sergis, and R. J. Wilson (2010), Nature of the ring current in Saturn's dayside magnetosphere, *J. Geophys. Res.*, *115*, A08201, doi:10.1029/2009JA015146.

### 1. Introduction

[2] The existence of an eastward-flowing ring current in Saturn's magnetosphere that distends the magnetic field lines outward from the planet was first inferred from Pioneer-11 and Voyager fly-by data, using magnetic field and plasma particle instrumentation [e.g., *Smith et al.*, 1980; *Ness et al.*, 1981; *Krimigis et al.*, 1983; *Richardson and Sittler*, 1990]. The magnetic perturbations were found to be well modeled by a simple four-parameter current disk, the parameters of which are the cylindrical radii of its inner and outer edges, its half thickness, and a parameter describing

the current density in the disk, assumed to fall inversely as the cylindrical radial distance from the magnetic axis [*Connerney et al.*, 1983]. Fits to the fly-by field data indicated a radial extent between  $\sim 8$  and  $\sim 16 R_S$ , a half thickness of  $2.5 R_S$ , and a total current near  $\sim 10 \text{ MA}$  ( $R_S$  is Saturn's equatorial radius, equal to 60,268 km). Recently, the same model, here termed the CAN (Connerney, Acuña, and Ness) model, has been applied to the more extensive data set obtained by the Cassini Saturn orbiter spacecraft. *Bunce et al.* [2007] studied magnetic field data from a set of near-equatorial Cassini orbits and showed that the strength and radial extent of the current both increase with the size of the magnetosphere under conditions of reducing solar wind dynamic pressure, thus, strongly influencing the magnetospheric response to the latter. *Kellett et al.* [2009] also studied north-south passes of the spacecraft through the ring current and showed that the half thickness is generally somewhat less than previously inferred, being  $\sim 1.5 R_S$  in the near-noon sector.

[3] Determination of the physical nature of Saturn's ring current, i.e., the actual combination of currents associated with the inertia of the near-corotating plasma and hot particle effects, has proved to be considerably more elusive. *McNutt* [1984] provided evidence that plasma inertia was important in the outer ring current during the Voyager-1 fly-by, while *Mauk and Krimigis* [1985] suggested that pressure gradient currents may be dominant within more

<sup>1</sup>Department of Physics and Astronomy, University of Leicester, Leicester, UK.

<sup>2</sup>Mullard Space Science Laboratory, University College London, Dorking, UK.

<sup>3</sup>Center for Planetary Sciences, University College London/Birkbeck, London, UK.

<sup>4</sup>Space and Atmospheric Physics Group, Imperial College, London, UK.

<sup>5</sup>Department of Physics and Astronomy, University of Iowa, Iowa City, Iowa, USA.

<sup>6</sup>Office for Space Research and Technology, Academy of Athens, Athens, Greece.

<sup>7</sup>Laboratory for Atmospheric and Space Physics, University of Colorado at Boulder, Boulder, Colorado, USA.

central regions. With the recent emergence of much more extensive plasma bulk parameter data from the Cassini spacecraft [e.g., *Sergis et al.*, 2007, 2009; *Lewis et al.*, 2008; *Schippers et al.*, 2008; *Wilson et al.*, 2008; *McAndrews et al.*, 2009; *Persoon et al.*, 2009], this centrally important issue can now be addressed in some detail. *Sergis et al.* [2010] have combined density and pressure values from a number of near-equatorial passes in the radial range 6–15  $R_S$  to show that the inertia current density, though partially offset by westward directed anisotropy currents, is larger than the pressure gradient current density in the inner part of that radial range, and vice versa in the outer part, with approximate equality at distances of  $\sim 9$ – $10 R_S$ . Related results have also been derived by *Achilleos et al.* [2010], who have developed a detailed empirically based model of force balance in Saturn's ring current region, though in this case the model suggests a resumption of dominant inertia currents in the outer region (at radial distances beyond  $\sim 12 R_S$ ), in line with the results of *Arridge et al.* [2007].

[4] The present paper addresses the issue of the nature of Saturn's ring current in a manner that is complementary to that of *Sergis et al.* [2010] and *Achilleos et al.* [2010], by examining plasma parameter profiles obtained by Cassini on individual passes through the region and comparing the current density profiles derived with CAN model fits to the magnetic field data from the pass. Data from more than 20 passes have been studied and are exemplified in this paper by a detailed discussion of two consecutive passes through the dayside ring current, on Revs 15 and 16 in September and October 2005 (a detailed study of the full data set is currently in preparation). These passes are closely equatorial, with latitudes that deviate from zero by at most  $0.3^\circ$  in the region of interest and are distinguished amongst the near-equatorial Cassini orbits by providing the maximum radial coverage to date, between  $\sim 3$  and  $\sim 20 R_S$ . The passes thus span the radial range from the Enceladus plasma torus in the inner region to the vicinity of the dayside magnetopause. Otherwise, analysis of the magnetic field data by *Bunce et al.* [2007] indicates that the ring current conditions on these passes are not unusual.

## 2. Plasma Current Density

[5] The current density perpendicular to the magnetic field  $\mathbf{B}$  flowing in a magnetized plasma can be expressed in terms of the plasma parameters [e.g., *Vasyliunas*, 1984] by

$$\mathbf{j}_\perp = \frac{\mathbf{B}}{B^2} \times \left[ \rho_m \frac{d\mathbf{V}}{dt} + \nabla P_\perp + (P_\parallel - P_\perp)(\hat{\mathbf{b}} \cdot \nabla) \hat{\mathbf{b}} \right], \quad (1)$$

where  $\rho_m$  is the plasma mass density,  $\mathbf{V}$  is the bulk speed,  $\hat{\mathbf{b}} = \mathbf{B}/B$  is the unit vector along the field, and  $P_\parallel$  and  $P_\perp$  are the field-parallel and perpendicular plasma pressures, respectively. The first term on the right side is the inertia current, the second the pressure gradient current, and the third the anisotropy current. The latter term goes to zero in the limit of isotropic pressure  $P_\parallel = P_\perp = P$ .

[6] To take the analysis further, we assume approximate axial symmetry ( $\partial/\partial\phi \equiv 0$ ) and that the observations are made exactly on the planet's spin equator (a very good approximation), such that parameter variations are due principally to radial gradients. We expect that these

assumptions should be well satisfied in the inner part of the system dominated by warm ( $\sim 10$ – $1$  keV) plasma and the planetary field but may be more questionable at larger distances where variable structured hot (tens of keV) plasma becomes important as observed in energetic neutral atom images [e.g., *Krimigis et al.*, 2007; *Mitchell et al.*, 2009], and the field has local time dependency associated with the day-night asymmetry. Even so, the principal gradients will still generally be those in the meridian, thus, justifying axial symmetry as an appropriate approximation for initial study. We also correspondingly assume that the plasma velocity is purely azimuthal about the coaligned spin and magnetic axes, with speed  $V_\phi$ . However, we make no further assumption about the direction of the magnetic field, such that in general, we take  $\hat{\mathbf{b}} = (b_r, b_\theta, b_\phi)$ . While clearly the principal field component in the equatorial region will generally be the colatitudinal component, such that  $b_\theta \approx 1$ , significant, but not dominant, radial and azimuthal fields may also occur in the outer part of the system (beyond  $\sim 12 R_S$ ). Persistent radial fields are due to the northward displacement of the magnetic equator from the spin equator due to solar wind forcing effects under the southern summer conditions prevailing [*Arridge et al.*, 2008a], while azimuthal fields may be produced by field sweepback effects in the presence of subcorotating flow. With these assumptions, equation (1) then yields the following expression for the azimuthal component of the field-perpendicular current density

$$j_{\perp\phi} \approx \frac{1}{B} \left[ \frac{\rho_m V_\phi^2 b_\theta}{r} - (1 - b_\phi^2) \left( \frac{1}{b_\theta} \frac{\partial P_\perp}{\partial r} + \frac{(P_\perp - P_\parallel)}{R} \right) \right], \quad (2)$$

where  $r$  is radial distance from the spin/magnetic axis, and  $R$  is the local radius of curvature of the field lines. Equation (2) neglects a small term in the pressure gradient current that contains the pressure anisotropy and the square of the radial field and additional small terms in the pressure anisotropy current that contain the azimuthal field and its spatial derivatives. Of the quantities in equation (2), only the field radius of curvature  $R$  in the anisotropy current cannot be directly determined from near-equatorial data. However, the pressure anisotropies of main concern here are the strong  $P_\perp > P_\parallel$  anisotropies in the warm ion population in the inner part of the system, within  $\sim 10 R_S$ , as discussed in section 3. Inside such distances the field does not generally depart strongly from a near-dipolar field [*Bunce et al.*, 2008; *Arridge et al.*, 2008b], for which  $R = r/3$ . Here we will therefore use this value as a simple approximation in equation (2), recognizing that as the field becomes increasingly extended in the outer region by the plasma currents, the radius of curvature of the equatorial field will be reduced, and the anisotropy currents correspondingly enhanced compared with those calculated here.

[7] In addition to the plasma currents considered here, we note that *Wahlund et al.* [2009] have recently suggested that negatively charged ice grains associated with the E ring, moving in the inner magnetosphere in near-Kepler orbits, may also produce a significant westward azimuthal current. If so, the current would flow in a narrowly confined equatorial ring at a radial distance of  $\sim 4 R_S$  where the grain density sharply maximizes [e.g., *Kurth et al.*, 2006], close to

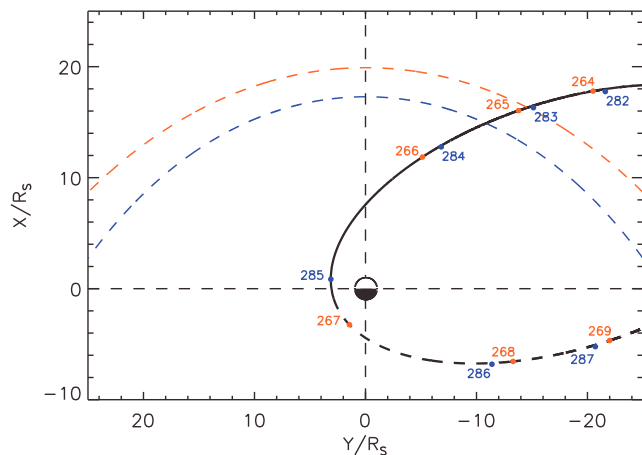


**Figure 1.** Cassini trajectory for Revs 15 and 16 shown in the planet’s equatorial ( $X$ - $Y$ ) plane, with noon at the top and dusk to the left. The trajectories of both Revs are represented by the thick black line where the solid and dashed sections represent the inbound and outbound parts of the orbits, respectively. The colored circles indicate day boundaries for Rev 15 (red) and Rev 16 (blue), which are marked with similarly color-coded “day of year” (2005) numbers. The red and blue dashed lines show model magnetopause positions for Revs 15 and 16, respectively, computed using the *Arridge et al.* [2006] model fitted to the last inbound magnetopause crossing.

the orbit of the moon Enceladus which is the source of the ice grains. Here we do not consider the physics of this suggestion but will comment further below on the empirical basis of the nature of the magnetic field perturbations observed.

### 3. Plasma Parameter Profiles

[8] As indicated in section 1, the data examined here were obtained on consecutive inbound Cassini orbits, Revs 15 and 16. Figure 1 shows the spacecraft trajectory in the planet’s equatorial  $X$ - $Y$  plane with the Sun at the top. The coordinate system employed is such that  $Z$  points along the planet’s spin axis, the  $X$ - $Z$  plane contains the Sun, and  $Y$  points toward dusk, completing the right-handed system. The trajectories of Revs 15 and 16 are closely similar, both being represented by the black line, where the solid and dashed portions represent the inbound and outbound parts of the orbits, respectively. Only the data from the inbound passes are examined here, the more complicated situation on the nightside being reserved for future study. The colored circles show day boundaries for Revs 15 (red) and 16 (blue), which are marked with similarly color-coded “day of year” (2005) numbers. The red and blue dashed lines show model magnetopause positions for Revs 15 and 16, respectively, computed using the *Arridge et al.* [2006] model fitted to the innermost magnetopause crossing observed on the pass.

[9] Given the assumptions discussed in section 2, all the parameters in equation (2) can in principle be determined, allowing estimates to be made of the local azimuthal current density on individual passes through the ring current, such as those shown in Figure 1. In practice, however, not all

parameters are routinely available, particularly those of the warm ion population, due to instrument field-of-view restrictions that are dependent on the orientation of the three-axis stabilized spacecraft. Where required, therefore, available data have been augmented with empirical models derived from particular data sets, as described below. In addition to data from the magnetic field instrument [*Dougherty et al.*, 2004], employed here at 1 min resolution, the data sets routinely available that are employed in this study are as follows.

[10] 1. Density and pressure data at 5 min resolution for hot ( $>3$  keV) protons ( $H^+$ ) and water group ions ( $W^+$ ) combined, derived from Magnetospheric Imaging Instrument (MIMI)/Charge Energy Mass Spectrometer (CHEMS) and Low Energy Magnetic Measurement System (LEMMS) data by integration over the energy range from 3 to  $>200$  keV, the water group ion spectrum being extrapolated to 3 keV from minimum measured energies of 9 keV [*Krimigis et al.*, 2004; *Sergis et al.*, 2007, 2009]. Pressure anisotropies are not presently available but are not believed to be large [*Sergis et al.*, 2009], such that the hot ion pressure is taken to be isotropic at all radial distances as in previous related works.

[11] 2. Density and pressure data at 1 min resolution for cold ( $T_e \sim 1-10$  eV) and warm ( $T_e \sim 100$  eV to 1 keV) electrons combined, obtained from Cassini Plasma Spectrometer (CAPS)/Electron Spectrometer (ELS) data by integration over the energy band from 0.6 eV to 26 keV [*Young et al.*, 2004; *Lewis et al.*, 2008; *Schippers et al.*, 2008]. The pressure is again taken to be isotropic. Valid parameters can only be derived in lower plasma density regions where the spacecraft potential is positive, typically beyond radial distances of  $\sim 10-12 R_S$ , the data then being corrected for the determined positive spacecraft potential with elimination of measured spacecraft photoelectrons. In inner regions of higher plasma density where the spacecraft potential becomes a few volts negative, the cold electron population is not fully measured. In these regions we instead use the CAPS/ELS data to compute the partial density and pressure of electrons with energy  $>20$  eV. Electrons with these energies are not strongly affected by the spacecraft potential, such that the partial densities and pressure  $>20$  eV provide valid information on the warmer electron population.

[12] 3. Total electron density measurements at 8–16 s resolution obtained from measurements of the upper hybrid resonance frequency by the RPWS instrument [*Gurnett et al.*, 2004; *Persoon et al.*, 2009]. These data are generally available between periapsis and radial distances of  $\sim 8-10 R_S$ .

[13] The methodology adopted is illustrated in Figure 2, where we show radial profiles of plasma density (Figure 2, top) and pressure (Figure 2, bottom) for the inbound passes of Revs 15 (Figure 2, left) and 16 (Figure 2, right), spanning  $\sim 3-20 R_S$ . The vertical dashed lines at a radial distance of  $18.8 R_S$  in the plots for Rev 16 show the last inbound magnetopause crossing, such that we do not consider data beyond that point. We first construct a radial profile of the total electron number density by combining RPWS data (yellow) in the inner region with CAPS/ELS data (blue) in the outer region where the spacecraft potential is positive. Similarly colored solid lines join values averaged over  $0.25 R_S$  intervals. A small data gap of  $\sim 1-2 R_S$  generally

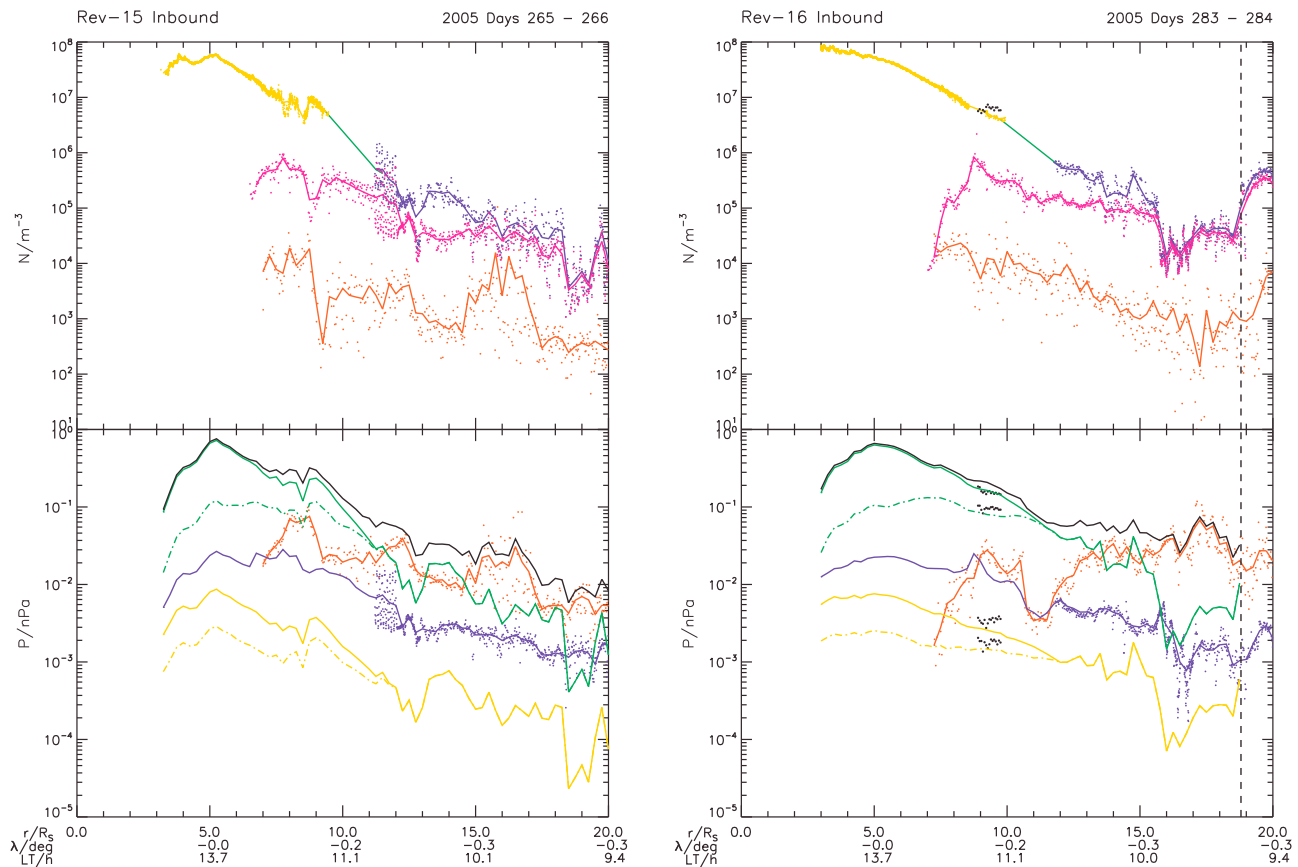


**Figure 2.** Profiles of particle density and pressure for (left) Rev 15 and (right) Rev 16 over the radial range from  $\sim 3$  to  $20 R_S$ . The vertical black dashed line at a radial distance of  $18.8 R_S$  for Rev 16 shows the last inbound magnetopause crossing. (top) Each plot shows the radial profile of the electron density ( $\text{m}^{-3}$ ). The yellow and blue data show the total number density from the RPWS and CAPS/ELS instruments, respectively. The similarly colored solid lines join values averaged over  $0.25 R_S$  intervals. The green solid line shows the log-linear interpolation between these two data sets. The magenta data show the partial density of warm ( $>20$  eV) electrons from the CAPS/ELS instrument, while the red data show the hot ( $>3$  keV) ion density obtained from the MIMI instrument (water group ions and protons combined). (bottom) Each plot shows the related radial profiles of the plasma pressure (nPa). The red data show the hot ( $>3$  keV) ion pressure from the MIMI instrument, while the blue data show the electron pressure from CAPS/ELS. The green and yellow solid lines show the perpendicular pressure of the warm water group ions and protons, respectively, while the similarly colored dot-dashed lines show the parallel pressures of these populations. The total perpendicular pressure is shown by the solid black line. The black points for (right) Rev 16 show a small number of warm ion density and pressure values derived from CAPS/IMS data by *Wilson et al.* [2008]. Spacecraft radial distance ( $R_S$ ) is shown at the bottom of the plot, together with the latitude (degrees) and local time (hours).

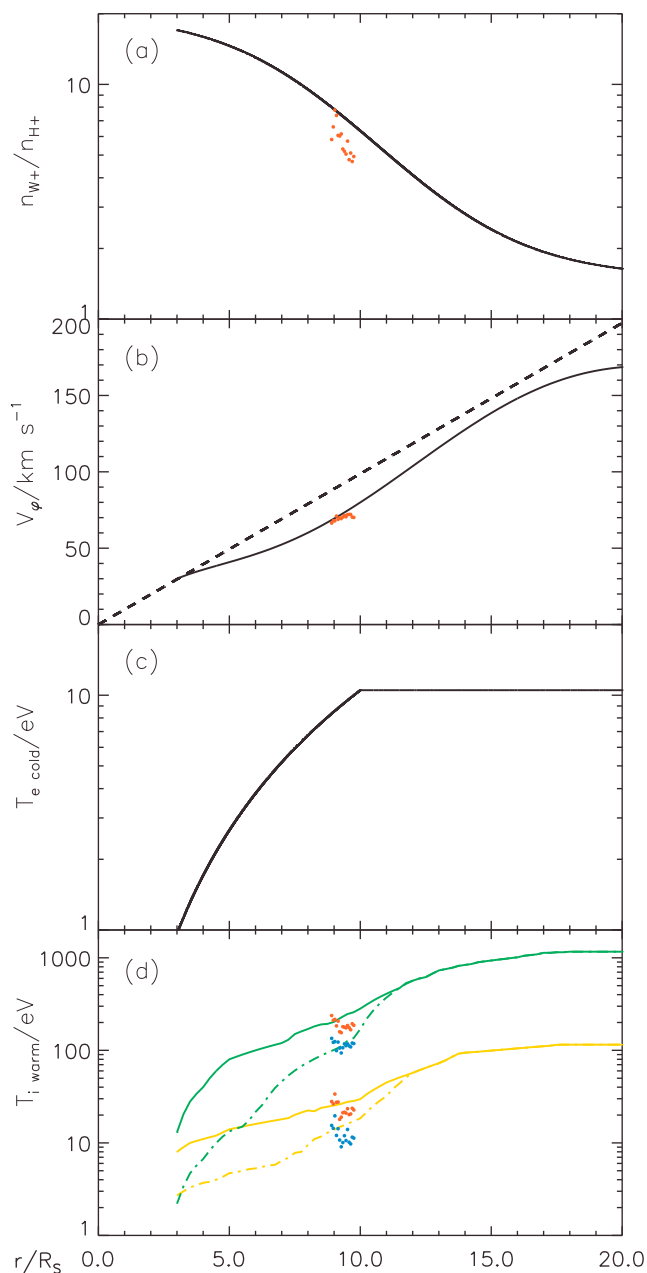
remains between the RPWS and CAPS/ELS density data, centered near  $\sim 10 R_S$ , which we close by log-linear interpolation shown by the green line.

[14] The magenta data in the upper panels show the partial density of  $>20$  eV electrons as described above, extending into the inner region where the spacecraft potential becomes negative, but truncated and set to zero in the innermost region (where the density is much less than the total) because of contamination of the CAPS/ELS data by penetrating radiation belt particles. The difference in density between these values and the total electron density is taken to be the density of the cold ( $T_e \sim 1\text{--}10$  eV) electrons. By charge neutrality, the total electron density shown in

Figure 2 (top) is also the total ion density (the charge density of charged ice grains generally being negligible), assuming the ions are predominantly singly charged. The red data in Figure 2 (top) show the hot ( $>3$  keV) water group ion plus proton density obtained by integration of the MIMI data, such that the difference between these values and the total density then represents the density of the warm ( $<3$  keV) ions. The hot ion values are also truncated and set to zero in the inner region (where they are also much less than the total) for reasons similar to the electron data. It can be seen that except for some regions in the outer magnetosphere, the hot ions represent  $\sim 1\%$  or less of the total ion density, such that the vast majority of the ions belong to the warm pop-

ulation. The black points at radial distances of  $\sim 9\text{--}10 R_S$  in the density panel for Rev 16 show a small number of warm ion density values derived from CAPS/IMS data on this pass by *Wilson et al.* [2008]. It can be seen that these values agree very well with the concurrent RPWS density data. No such determinations are available for Rev 15 because of a lack of suitable spacecraft orientation.

[15] The mass density of the plasma  $\rho_m$ , required for the inertia current, is then obtained by applying a model ratio  $R_i = (n_{W+}/n_{H+})$  of warm water group ions (mass 17 atomic mass unit (AMU)) and protons (mass 1 AMU) to the total density data. This model is shown in Figure 3a (which shows all the empirical model profiles employed here), obtained from the overall analyses of CAPS/IMS data presented by *Wilson et al.* [2008] and *McAndrews et al.* [2009]. The value of  $R_i$  decreases from  $\sim 15$  at  $\sim 5 R_S$ , to  $\sim 5$  at



$\sim 10 R_S$ , and to  $\sim 1.5$  at  $\sim 20 R_S$  and is in agreement with the few individual values derived for Rev 16 by *Wilson et al.* [2008], shown by the red points in the plot. The moderately subcorotational azimuthal velocity of the plasma  $V_\phi$  required for the inertia current has been taken from the empirical model employed by *Achilleos et al.* [2010], based on the overall results of *Wilson et al.* [2008] and *Kane et al.* [2008]. This model is shown in Figure 3b, where the dashed straight line shows rigid corotation for comparison. The model is again in good agreement with the Rev 16 data derived by *Wilson et al.* [2008] shown by the red points. These values are then combined with magnetic data to derive the inertia current density in equation (2).

[16] We now turn to the pressure profiles shown in Figure 2 (bottom). The red data show the hot ( $>3$  keV) ion pressure for water group ions and protons combined, derived from MIMI data, which make a small contribution to the total pressure inside  $\sim 8 R_S$  but dominate the total pressure beyond  $\sim 15 R_S$ . The blue data show the electron pressure, determined by direct integration in the outer region where the spacecraft potential is positive, and by combining the  $>20$  eV partial electron pressure with an estimate of the cold electron pressure in the inner region where the spacecraft potential is negative. The cold electron pressure has been determined by combining the difference between the  $>20$  eV and total electron densities shown in the upper panels, with the cold electron temperature model of *Persoon et al.* [2009], shown in Figure 3c. In this model, the cold electron temperature increases from  $\sim 1$  eV at  $\sim 3 R_S$  to  $\sim 10$  eV at  $\sim 10 R_S$ , where we note that we have slightly extrapolated the original model of *Persoon et al.* [2009] from an inner limit of  $3.5 R_S$  to cover the whole range to  $3 R_S$  considered here. Beyond  $10 R_S$ , the cold electron temperature is taken to remain constant at  $\sim 10$  eV on the basis of the results pre-

**Figure 3.** Plots of empirical model plasma parameter profiles employed to estimate the quantities required to derive the plasma currents. The continuous lines in the figure show models of (a) the number density ratio of warm water group ions and protons obtained from *Wilson et al.* [2008] and *McAndrews et al.* [2009]; (b) the azimuthal velocity of the plasma from the empirical model of *Achilleos et al.* [2010] based on the results of *Wilson et al.* [2008] and *Kane et al.* [2008] (the dashed line corresponds to rigid corotation with the planet); (c) the cold electron temperature model of *Persoon et al.* [2009], extrapolated to  $3 R_S$  from an inner boundary of  $3.5 R_S$ , and extended at constant value beyond  $10 R_S$  on the basis of the results of *Schippers et al.* [2008]; and (d) the field-perpendicular (solid lines) and field-parallel (dot-dashed lines) temperatures of warm water group ions (green) and protons (yellow), derived for radial distances beyond  $\sim 5.5 R_S$  by *Wilson et al.* [2008] and *McAndrews et al.* [2009] and augmented in the inner region ( $\sim 3\text{--}5 R_S$ ) using Voyager data modeled by *Richardson* [1995]. The individual data points in the panels show warm ion data derived by *Wilson et al.* [2008] from CAPS/IMS observations specifically for Rev 16, where in Figure 3d, the red points correspond to the perpendicular temperature and the blue points correspond to the parallel temperature.

sented by *Schippers et al.* [2008]. The 20 eV cutoff in the warm electron integrations was thus chosen to approximately interface with these values without a significant gap or overlap. The total electron pressure in Figure 2 is seen to peak at  $\sim 5\text{--}7 R_S$  where the cold electrons dominate and falls gradually with increasing distance in the outer region where the warm electrons dominate. Overall, the electron pressure throughout is  $\sim 10\%$  or less of the total perpendicular pressure (shown by the solid black line).

[17] The green and yellow solid lines in Figure 2 (bottom) then show the perpendicular pressures of the warm water group ions and protons, respectively. These have been determined by combining the warm ion number densities estimated as above with the perpendicular ion temperature models shown by the corresponding green and yellow solid lines in Figure 3d. The temperature profiles have been obtained from smoothed CAPS/IMS data derived by *Wilson et al.* [2008] and *McAndrews et al.* [2009] for radial distances beyond  $\sim 5.5 R_S$ , which have been augmented in the inner region ( $\sim 3\text{--}5 R_S$ ) with Voyager data modeled by *Richardson* [1995] that interface well with the Cassini data. The temperatures increase with radial distance, lying typically in the range  $\sim 10\text{--}100$  eV for protons and  $\sim 100$  eV to 1 keV for water group ions, thus, again approximately interfacing with the hot ( $>3$  keV) ion data without a significant gap or overlap. The small number of perpendicular temperatures determined on Rev 16 by *Wilson et al.* [2008] (red data in Figure 3) again agree very well with the overall temperature model, such that the corresponding perpendicular pressures (black data in Figure 2, bottom) also agree very well with the overall estimates.

[18] Our results show that while the warm proton pressure (yellow) is negligible throughout, being  $\sim 1\%$  of the total, the warm water group ion perpendicular pressure (green) dominates in the inner region, peaking at  $\sim 1$  nPa at  $\sim 5\text{--}6 R_S$ . Its value then falls to become comparable to the hot ion pressure (red) in the range  $\sim 12\text{--}15 R_S$ , before becoming smaller than the latter beyond  $\sim 15 R_S$ , in agreement with the previous results of *Sergis et al.* [2010]. The total perpendicular pressure profile, obtained by summing the contributions of the various populations is then shown by the black solid line, from which the pressure gradient current density in equation (2) is derived in section 4. It peaks with the warm water group ions in the inner region and falls gradually in the outer region in a manner determined principally by the combined behavior of the hot and warm ions.

[19] A significant feature of the warm ion populations is that their distributions are strongly anisotropic in the inner region with  $P_{\perp} > P_{\parallel}$ , as shown by both Voyager and Cassini ion data [*Richardson and Sittler*, 1990; *Richardson*, 1995; *Wilson et al.*, 2008], though approaching isotropy beyond  $\sim 12 R_S$ . The parallel pressures of these populations are shown by the dot-dashed green and yellow lines in Figure 2 (bottom), again obtained by combining the warm ion density profiles for water group ions and protons with the parallel temperature model shown by the corresponding dot-dashed green and yellow lines in Figure 3d. These model temperatures have been determined in the same way as for the perpendicular temperature models described above. The parallel temperature values derived for Rev 16 by *Wilson et al.* [2008] are shown by the blue data in Figure 3d,

corresponding to the parallel pressure values shown by the black data in Figure 2 (bottom). The pressure anisotropies of these populations are those employed here to determine the anisotropy current density in equation (2). As mentioned above, pressure anisotropy profiles of the hot ions and the electrons are not presently available, being generally difficult to determine because of variably incomplete pitch angle coverage. However, examination of hot ion distributions observed during spacecraft roll maneuvers in the central ring current region on Revs 15 and 16 indicate the presence of distributions that differ from isotropy only by a few tens of percent, while electrons beyond  $\sim 10 R_S$  exhibit field-aligned distributions with pressure ratios  $P_{\parallel}/P_{\perp} \sim 2$  or less. As indicated in section 4 below, the anisotropy currents produced by these populations will generally be more than an order of magnitude less than the current sources included here. The warm ions are thus expected to produce the most important anisotropy effects within the ring current, with pressure ratios ( $P_{\perp}/P_{\parallel}$ )  $\approx 5$  for the dominant water group ions in the inner region.

#### 4. Current Density Profiles

[20] Given the data shown in Figure 2, we can now compute the current density profile from equation (2) and compare it to that deduced from CAN disk modeling of the observed magnetic field perturbations. Results are shown in Figure 4 for Revs 15 (left) and 16 (right). Figure 4 (top) shows the CAN model fits (gray dashed lines) to the colatitudinal component of the magnetic data (blue), from which the ‘‘Cassini SOI’’ internal field model has been subtracted [*Dougherty et al.*, 2005]. The residual field results principally from the ring current and shows strong negative values of  $\sim 10$  to  $15$  nT in the inner region ( $<8 R_S$ ), reversing to weaker positive values in the outer region ( $>15 R_S$ ). The methodology employed to obtain the CAN model fits follows that of *Bunce et al.* [2007], except that here we have used a current sheet half thickness of  $1.5 R_S$ , instead of  $2.5 R_S$  in the former study, following the results of *Kellett et al.* [2009] concerning the thickness of the current sheet in the dayside sector. The remaining three fit parameters for Rev 15 are inner and outer radii of  $6.75$  and  $17.5 R_S$ , respectively, and a current density parameter,  $\mu_0 J_0 = 55.0$  nT (the current density within the current disk being given by  $j_{\phi} = I_0/\rho$ , where  $\rho$  is the perpendicular distance from the magnetic/spin axis), while for Rev 16 these parameters are  $7.5$  and  $17.5 R_S$  and  $64.0$  nT, respectively. The resulting fits to the data are seen to be reasonably good in both cases, with RMS deviations of  $2.07$  and  $2.10$  nT for Revs 15 and 16, respectively. The implied equatorial current density profile is shown by the gray dashed line in the bottom panel, for comparison with the estimated plasma current density profiles.

[21] We note in passing at this point that there is no evidence in these (or other) magnetic field data for significant currents associated with charged E ring grains as suggested by *Wahlund et al.* [2009]. As mentioned in section 2, these would produce an equatorial ring of eastward (positive azimuthal) current at a radial distance near  $\sim 4 R_S$  where the grain density sharply maximizes, which will produce negative perturbations in the colatitudinal field inside this dis-

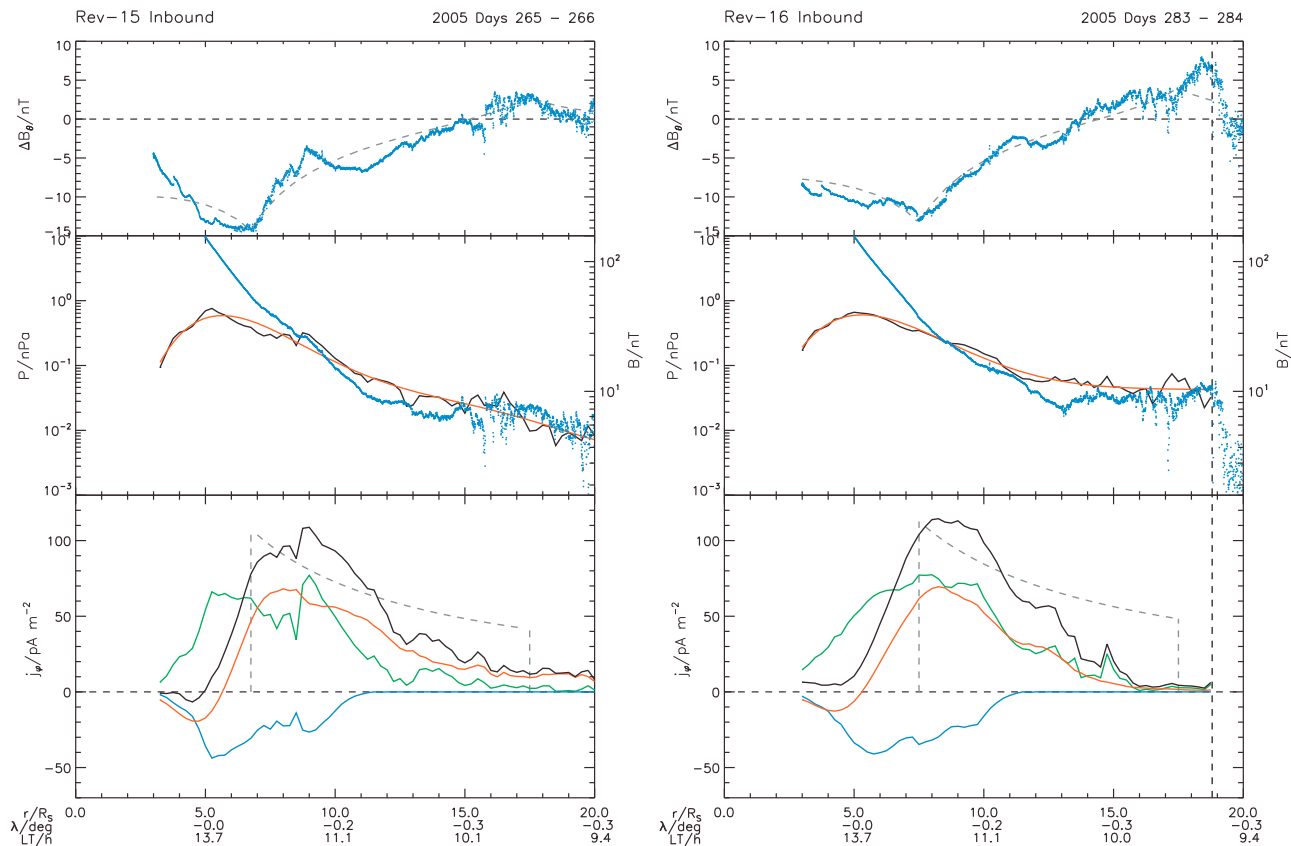


**Figure 4.** Radial profiles of the magnetic field, pressure, and current density for (left) Revs 15 and (right) Rev 16. (top) Each plot shows the colatitudinal component of the magnetic field (nT) from which the “Cassini SOI” model of the internal field has been subtracted (blue). The CAN model fit to these data is shown by the gray dashed line. (middle) Each plot shows total perpendicular plasma pressure obtained from Figure 2 (bottom) (black), a fifth-order polynomial fit to this data (red) and the magnetic pressure (blue). A magnetic field strength scale is also shown on the right side. (bottom) Each plot shows current density profiles. The green line shows the inertia current density, the red line shows the pressure gradient current density, and the blue line shows the anisotropy current density, while the black line shows the sum of these three, i.e., the total current density. The gray dashed line shows the equatorial current density profile obtained from the CAN modeling of the magnetic field on these passes.

tance, reversing sharply to positive perturbations outside this distance. Clearly no such perturbations are observed in Figure 4 (top), at least within the  $\sim 1$  nT level of general field fluctuations. Biot-Savart considerations then show that the upper limit to such a current is  $\sim 0.4$  MA, which may be compared with the total plasma ring current of  $\sim 8$  MA implied by the CAN modeling of the observed field perturbations for both Revs 15 and 16 above.

[22] Figure 4 (middle) then shows comparisons between the total perpendicular plasma pressure (black), obtained from Figure 2 (bottom), with the magnetic pressure (blue), such that their ratio gives the local plasma  $\beta$  value. It can be seen that  $\beta$  is small in the inner region but increases to unity at  $\sim 8$ – $9 R_S$  where the field and plasma pressures are near equal, while  $\beta > 1$  conditions are maintained throughout the outer magnetosphere, as found previously by *Sergis et al.* [2010]. The red lines show fifth-order polynomial fits to the perpendicular pressure profiles, which have then been used to determine the pressure gradient current in equation (2). The polynomial profile is seen to provide a

good overall fit to the pressure data in each case, while smoothing over small-scale structure in the data.

[23] Current density profiles resulting from each term in equation (2) are shown in Figure 4 (bottom), where the green line shows the inertia current density, the red line shows the pressure gradient current density, and the blue line shows the anisotropy current density. The black line shows the sum of these three, for comparison with the CAN model profile shown by the gray dashed line. It can be seen that the pressure gradient current (red) is small and is negative in the innermost region where the pressure increases with radius, passes through zero at  $\sim 5$ – $6 R_S$  where the total perpendicular pressure peaks (solid black line in Figure 4, middle), peaks at  $\sim 7$ – $8 R_S$  near the inner edge of the CAN model profile, and then falls with distance in the outer magnetosphere, more quickly for Rev 16 than Rev 15 because of the weaker radial gradient in the former pressure profile than in the latter. By contrast, the inertia current, which is positive throughout, rises rapidly from small values in the innermost region at  $\sim 3 R_S$ , to values much larger than

that of the pressure gradient current in the inner region out to  $\sim 7 R_S$ , as found by *Sergis et al.* [2010]. It then peaks around  $\sim 7\text{--}9 R_S$  before falling again in the outer region. The outer values are similar on the two passes, being comparable with the smaller outer pressure gradient currents on Rev 16, while being lower than the higher pressure gradient currents on Rev 15.

[24] The blue lines in Figure 4 (bottom) show the anisotropy current densities for the two passes determined from the warm ion populations, which are negative and of significant magnitude throughout the inner region because of the  $P_\perp > P_\parallel$  conditions prevailing. It can be seen that in the innermost region between  $\sim 4$  and  $\sim 7 R_S$ , these currents are approximately equal and opposite to the inertia currents, such that the anisotropy current strongly modifies the current profile in the inner region. Beyond  $\sim 7 R_S$ , however, these currents gradually decline to smaller values as the warm ion pressures approach isotropy and are zero within our estimates beyond  $\sim 12 R_S$  where the pressures are isotropic. Because of the approximate cancellation between the inertia current and the pressure anisotropy current in the inner region ( $< 6 R_S$ ), the total current curve shown by the black line in Figure 4 (bottom) more nearly follows the pressure gradient current in this region. As the anisotropy current declines in strength in the region beyond ( $> 7 R_S$ ), however, the total current increases, following a similar profile to the pressure gradient current but with values that are a factor of  $\sim 1.5$  greater than the latter in the case of Rev 15, increasing to  $\sim 2$  times greater for Rev 16.

[25] With regard to the anisotropy currents of hot ions and electrons in the central and outer ring current region, neglected here, we note that estimates based on equation (2) show that the hot ion departures from isotropy of a few tens of percent indicated in section 3 will produce anisotropy currents of typically  $\sim 2 \text{ pA m}^{-2}$ , smaller by more than an order of magnitude than the currents estimated here. Similarly, while electron pressure anisotropies  $P_\parallel/P_\perp \sim 2$  in the outer region may typically be somewhat larger, the estimated anisotropy currents remain at similar low values because the electron pressures are typically  $\sim 10\%$  of the ion pressures. Inclusion of these effects, while desirable in future work, is thus unlikely to change our overall conclusions.

[26] Comparing with the CAN model profiles, we observe significant correspondences, with both currents peaking at similar values of  $\sim 100 \text{ pA m}^{-2}$ . The peak values deduced from the plasma data occur at radial distances of  $\sim 8\text{--}9 R_S$ , just outside the  $\sim 7 R_S$  inner edges of the best fit disk models, with values decreasing rapidly at smaller radial distances. Beyond the peak, however, the current deduced from the plasma data decreases more rapidly with increasing radial distance than is assumed in the disk model, as previously noted by *Sergis et al.* [2010].

## 5. Summary and Discussion

[27] Following the recent discussion by *Sergis et al.* [2010] of average conditions within Saturn's central ring current region ( $6\text{--}15 R_S$ ) deduced from plasma data obtained by the Cassini spacecraft, here we have presented a first complementary discussion of the ring current densities over the radial range  $\sim 3$  to  $\sim 20 R_S$  on two individual near-

equatorial dayside passes. Magnetic field and plasma data from 20 additional passes have been studied with similar results and will be the subject of a more extended paper to follow. Here we have also compared the results with those obtained for the same passes from modeling the observed magnetic perturbations using the *Connerney et al.* [1983] current disk model, following the methodology of *Bunce et al.* [2007]. We have first shown that although the inertia current density associated with warm water group ions is the largest individual current component inside radial distances of  $\sim 6 R_S$ , the eastward current due to this component is strongly reduced in this region by the oppositely directed westward current because of the strong  $P_\perp > P_\parallel$  pressure anisotropy of these ions, such that these currents approximately cancel inside this distance. The total current density in the inner region then more nearly follows the pressure gradient current density, rising quite sharply from near-zero values near  $\sim 6 R_S$  and peaking at  $\sim 8 R_S$ .

[28] We suggest that the physical origin of this near-cancellation effect results from the nature of the warm water ion source, which is believed to be due to charge exchange-related ion pickup from the Enceladus-related torus of water group neutral particles that orbit Saturn [e.g., *Tokar et al.*, 2008]. Ion pickup from a cold neutral source which is orbiting with a Keplerian speed  $V_K$ , significantly less than the near-corotation speed of the plasma  $V_\phi$ , produces a strong pressure anisotropy with  $P_\perp > P_\parallel$ , for which it is easy to show that the inertia and anisotropy currents are approximately equal and opposite in a quasi-dipolar field. Putting  $R \approx r/3$  into equation (2) for a quasi-dipolar field and neglecting factors close to unity, the magnitude of the ratio of the anisotropy current density  $j_{\perp\phi A}$  to the inertia current density  $j_{\perp\phi I}$  is

$$\frac{|j_{\perp\phi A}|}{|j_{\perp\phi I}|} \approx \frac{3(P_\perp - P_\parallel)}{\rho_m V_\phi^2}. \quad (3)$$

Ion pickup under the above circumstances results in the formation of a ring distribution in velocity space in the plasma bulk flow frame, the ring being located at the field-perpendicular difference speed ( $V_\phi - V_K$ ) for all ion components, with near-zero speed parallel to the field lines. For such distributions, we have  $P_\perp \approx \rho_m (V_\phi - V_K)^2/2 \gg P_\parallel$ , such that equation (3) gives  $|j_{\perp\phi A}/j_{\perp\phi I}| \approx 3(1-f)^2/2$ , where  $f = (V_K/V_\phi)$ . The two current densities will thus generally be of comparable magnitude but opposite in direction. For example, in the cold plasma torus at a radial distance of  $\sim 5 R_S$ , the Kepler speed of the neutrals is  $\sim 11 \text{ km s}^{-1}$ , compared with our empirically based model plasma speed (at  $\sim 85\%$  of rigid corotation) of  $\sim 41 \text{ km s}^{-1}$ . We then have  $f \approx 0.27$  and  $|j_{\perp\phi A}/j_{\perp\phi I}| \approx 0.8$ , comparable with our results in the inner region shown in Figure 4. The ratio of these currents computed from the results shown in Figure 4 rises from values of  $\sim 0.3$  at a radial distance of  $\sim 3 R_S$  to peak at  $\sim 0.7$  at  $\sim 5.5 R_S$ , then falling to near zero at  $\sim 11 R_S$  where the warm ions become near isotropic.

[29] The cancellation effect is thus reduced at larger distances where the water group ions become scattered toward isotropy, such that beyond  $\sim 6 R_S$  the growing positive difference between the inertia and anisotropy currents significantly augments the pressure gradient current. Overall, the

equatorial radial profile of the eastward current density is similar in shape to that produced by the pressure gradient current alone but augmented in strength by factors of  $\sim 1.5$ – $2.0$ . In the two examples investigated here, which exhibit magnetic field perturbations that are entirely typical of the Cassini data set as a whole [Bunce *et al.* 2007], the total azimuthal current density rises from small values near  $\sim 6 R_S$ , peaks at  $\sim 100 \text{ pA m}^{-2}$  near  $\sim 8 R_S$ , and then falls more slowly with radial distance in the outer magnetosphere, reducing to values below  $\sim 25 \text{ pA m}^{-2}$  at distances beyond  $\sim 15 R_S$ , up to the  $20 R_S$  limit of our study. Estimates of the anisotropy currents of the hot ions and plasma electrons in the central and outer ring current, not included here, are more than an order of magnitude below such values. The similarity of the results obtained on the two passes, on nearly identical trajectories but separated in time by  $\sim 18$  days, again suggests that the results reflect typical conditions within Saturn's dayside magnetosphere. However, future work using a larger data set is required to test this conclusion. Comparison with the results of current disk modeling of the magnetic field perturbations on these passes shows good agreement with the gross features, particularly with the locations and magnitude of the peak current density. However, the currents derived from the plasma data are found to fall more rapidly with distance beyond the peak than the  $1/r$  dependence assumed in the model.

[30] Finally, no evidence is found for a current ring at a radial distance of  $\sim 4 R_S$  associated with the charged Kepler-rotating ice grains associated with the E ring, as suggested by Wahlund *et al.* [2009]. The magnetic data suggest an upper limit on such a current of  $\sim 0.4 \text{ MA}$ , compared with  $\sim 8 \text{ MA}$  in the outer plasma-produced ring current.

[31] **Acknowledgments.** Work at Leicester was supported by STFC grants PP/E000983/1, PP/D002117/1, and PP/E001130/1. S. K. was supported by a STFC Quota Award and wishes to thank N. Achilleos for useful discussions. M.K.D. was supported by STFC funding to Imperial College. The Cassini radio and plasma wave research at the University of Iowa was supported by NASA through JPL contract 1279973. Work at UCL-MSSL was supported by STFC grants PP/E001173/1 and PP/D00084X/1. C.S.A. was supported by a STFC Postdoctoral Fellowship and acknowledges useful discussions with G.R. Lewis. Work at the Academy of Athens was supported by subcontract 950782 with the JHU/APL. We thank S. Kellock and the Cassini team at Imperial College for access to the processed magnetic field data, G.R. Lewis and L.K. Gilbert for CAPS/ELS processing at MSSL, S.M. Krimigis for facilitating the use of MIMI data, and M.F. Thomsen and H.J. McAndrews for access to ion moment data.

[32] Masaki Fujimoto thanks Donald Mitchell and another reviewer for their assistance in evaluating this paper.

## References

- Achilleos, N., P. Guio, and C. S. Arridge (2010), A model of force balance in Saturn's magnetodisc, *Mon. Not. R. Astron. Soc.*, *401*, 2349–2371.
- Arridge, C. S., N. Achilleos, M. K. Dougherty, K. K. Khurana, and C. T. Russell (2006), Modeling the size and shape of Saturn's magnetopause with variable dynamic pressure, *J. Geophys. Res.*, *111*, A11227, doi:10.1029/2005JA011574.
- Arridge, C. S., C. T. Russell, K. K. Khurana, N. Achilleos, N. André, A. M. Rymer, M. K. Dougherty, and A. J. Coates (2007), Mass of Saturn's magnetodisc: Cassini observations, *Geophys. Res. Lett.*, *34*, L09108, doi:10.1029/2006GL028921.
- Arridge, C. S., K. K. Khurana, C. T. Russell, D. J. Southwood, N. Achilleos, M. K. Dougherty, A. J. Coates, and H. K. Leinweber (2008a), Warping of Saturn's magnetospheric and magnetotail current sheets, *J. Geophys. Res.*, *113*, A08217, doi:10.1029/2007JA012963.
- Arridge, C. S., C. T. Russell, K. K. Khurana, N. Achilleos, S. W. H. Cowley, M. K. Dougherty, D. J. Southwood, and E. J. Bunce (2008b), Saturn's magnetodisc current sheet, *J. Geophys. Res.*, *113*, A04214, doi:10.1029/2007JA012540.
- Bunce, E. J., S. W. H. Cowley, I. I. Alexeev, C. S. Arridge, M. K. Dougherty, J. D. Nichols, and C. T. Russell (2007), Cassini observations of the variation of Saturn's ring current parameters with system size, *J. Geophys. Res.*, *112*, A10202, doi:10.1029/2007JA012275.
- Bunce, E. J., C. S. Arridge, S. W. H. Cowley, and M. K. Dougherty (2008), Magnetic field structure of Saturn's dayside magnetosphere and its mapping to the ionosphere: Results from ring current modeling, *J. Geophys. Res.*, *113*, A02207, doi:10.1029/2007JA012538.
- Connerney, J. E. P., M. H. Acuña, and N. F. Ness (1983), Currents in Saturn's magnetosphere, *J. Geophys. Res.*, *88*, 8779–8789.
- Dougherty, M. K., et al. (2004), The Cassini Magnetic Field Investigation, *Space Sci. Rev.*, *114*, 331–383.
- Dougherty, M. K., et al. (2005), Cassini magnetometer observations during Saturn orbit insertion, *Science*, *307*, 1266–1270.
- Gurnett, D. A., et al. (2004), The Cassini Radio and Plasma Wave Investigation, *Space Sci. Rev.*, *114*, 395–463.
- Kane, M., D. G. Mitchell, J. F. Carbary, S. M. Krimigis, and F. J. Cray (2008), Plasma convection in Saturn's outer magnetosphere determined from ions detected by the Cassini INCA experiment, *Geophys. Res. Lett.*, *35*, L04102, doi:10.1029/2007GL032342.
- Kellett, S., E. J. Bunce, A. J. Coates, and S. W. H. Cowley (2009), Thickness of Saturn's ring current determined from north-south Cassini passes through the current layer, *J. Geophys. Res.*, *114*, A04209, doi:10.1029/2008JA013942.
- Krimigis, S. M., J. F. Carbary, E. P. Keath, T. P. Armstrong, L. J. Lanzerotti, and G. Gloeckler (1983), General characteristics of hot plasma and energetic particles in the Saturnian magnetosphere: Results from the Voyager spacecraft, *J. Geophys. Res.*, *88*, 8871–8892.
- Krimigis, S. M., et al. (2004), Magnetospheric Imaging Instrument (MIMI) on the Cassini Mission to Saturn/Titan, *Space Sci. Rev.*, *114*, 233–329.
- Krimigis, S. M., N. Sergis, D. G. Mitchell, D. C. Hamilton, and N. Krupp (2007), A dynamic, rotating ring current around Saturn, *Nature*, *450*, 1050–1053, doi:10.1038/nature06425.
- Kurth, W. S., T. F. Averkamp, D. A. Gurnett, and Z. Wang (2006), Cassini RPWS observations of dust in Saturn's E ring, *Planet. Space Sci.*, *54*, 988–998.
- Lewis, G. R., N. André, C. S. Arridge, A. J. Coates, L. K. Gilbert, D. R. Linder, and A. M. Rymer (2008), Derivation of density and temperature from the Cassini-Huygens CAPS electron spectrometer, *Planet. Space Sci.*, *56*, 901–912.
- Mauk, B. H., and S. M. Krimigis (1985), Particle and field stress balance within a planetary magnetosphere, *J. Geophys. Res.*, *90*, 8253–8264.
- McAndrews, H. J., et al. (2009), Plasma in Saturn's nightside magnetosphere and the implications for global circulation, *Planet. Space Sci.*, *57*, 1714–1722.
- McNutt, R. L., Jr. (1984), Force balance in outer planet magnetospheres, *Physics of Space Plasmas, Proc. 1982-4 MIT Symposia, SPI Conf. Proc. & Reprint Ser., vol. 5*, edited by J. Belcher et al., pp. 179–210, Scientific, Cambridge, Mass.
- Mitchell, D. G., et al. (2009), Recurrent energization of plasma in the mid-night-to-dawn quadrant of Saturn's magnetosphere, and its relationship to auroral UV and radioemissions, *Planet. Space Sci.*, *57*, 1732–1742.
- Ness, N. F., M. H. Acuña, R. P. Lepping, J. E. P. Connerney, K. W. Behannon, L. F. Burlaga, and F. Neubauer (1981), Magnetic field studies by Voyager 1: Preliminary results at Saturn, *Science*, *212*, 211–217.
- Persoon, A. M., et al. (2009), A diffusive equilibrium model for the plasma density in Saturn's magnetosphere, *J. Geophys. Res.*, *114*, A04211, doi:10.1029/2008JA013912.
- Richardson, J. D. (1995), An extended plasma model for Saturn, *Geophys. Res. Lett.*, *22*, 1177–1180.
- Richardson, J. D., and E. C. Sittler Jr. (1990), A plasma density model for Saturn based on Voyager observations, *J. Geophys. Res.*, *95*, 12,019–12,031.
- Schippers, P., et al. (2008), Multi-instrument analysis of electron populations in Saturn's magnetosphere, *J. Geophys. Res.*, *113*, A07208, doi:10.1029/2008JA013098.
- Sergis, N., S. M. Krimigis, D. G. Mitchell, D. C. Hamilton, N. Krupp, B. H. Mauk, E. C. Roelof, and M. Dougherty (2007), Ring current at Saturn: Energetic particle pressure in Saturn's equatorial magnetosphere measured with Cassini/MIMI, *Geophys. Res. Lett.*, *34*, L09102, doi:10.1029/2006GL029223.
- Sergis, N., S. M. Krimigis, D. G. Mitchell, D. C. Hamilton, N. Krupp, B. H. Mauk, E. C. Roelof, and M. K. Dougherty (2009), Energetic particle pressure in Saturn's magnetosphere measured with the Magnetospheric Imaging Instrument on Cassini, *J. Geophys. Res.*, *114*, A02214, doi:10.1029/2008JA013774.

- Sergis, N., et al. (2010), Particle pressure, inertial force and ring current density profiles in the magnetosphere of Saturn, based on Cassini measurements, *Geophys. Res. Lett.*, *37*, L02102, doi:10.1029/2009GL041920.
- Smith, E. J., L. Davis Jr., D. E. Jones, P. J. Coleman Jr., D. S. Colburn, P. Dyal, and C. P. Sonett (1980), Saturn's magnetosphere and its interaction with the solar wind, *J. Geophys. Res.*, *85*, 5655–5674.
- Tokar, R.L., et al. (2008), Cassini detection of water-group pickup ions in the Enceladus torus, *Geophys. Res. Lett.*, *35*, L14202, doi:10.1029/2008GL034749.
- Vasyliunas, V. M. (1984), Fundamentals of current description, in *Magnetospheric Currents*, edited by T. A. Potemra, *Geophys. Monogr.*, *28*, pp. 63–66, AGU, Washington, D. C.
- Wahlund, J.-E., et al. (2009), Detection of dusty plasma near the E ring of Saturn, *Planet. Space Sci.*, *57*, 1795–1806.
- Wilson, R. J., R. L. Tokar, M. G. Henderson, T. W. Hill, M. F. Thomsen, and D. H. Pontius Jr. (2008), Cassini plasma spectrometer thermal ion measurements in Saturn's inner magnetosphere, *J. Geophys. Res.*, *113*, A12218, doi:10.1029/2008JA013486.
- Young, D. T., et al. (2004), Cassini Plasma Spectrometer Investigation, *Space Sci. Rev.*, *114*, 1–112.
- C. S. Arridge and A. J. Coates, Mullard Space Science Laboratory, University College London, Dorking RH5 6NT, UK.
- E. J. Bunce, S. W. H. Cowley, and S. Kellett, Department of Physics and Astronomy, University of Leicester, Leicester LE1 7RH, UK. (sk175@ion.le.ac.uk)
- M. K. Dougherty, Space and Atmospheric Physics Group, Imperial College, London SW7 2BW, UK.
- A. M. Persoon, Department of Physics and Astronomy, University of Iowa, Iowa City, IA 52240, USA.
- N. Sergis, Office for Space Research and Technology, Academy of Athens, 11527, Athens, Greece GR-11527.
- R. J. Wilson, Laboratory for Atmospheric and Space Physics, University of Colorado at Boulder, Boulder, CO 80309, USA.